Actuation, Sensing, and Fabrication for In Vivo Magnetic Microrobots

K. Berk Yesin, Karl Vollmers, and Bradley J. Nelson

Institute of Robotics and Intelligent Systems
Swiss Federal Institute of Technology (ETH), Zurich
yesin@iris.mavt.ethz.ch, karl.vollmers@iris.mavt.ethz.ch, brad.nelson@iris.mavt.ethz.ch
http://www.iris.mavt.ethz.ch

Abstract. This paper investigates some of the fundamental design issues related to untethered biomedical microrobots guided inside the human body through external magnetic fields. Immediate application areas for these microrobots include cardiovascular, intraocular and inner-ear diagnosis and surgery. Issues investigated include the effects of magnetic actuation forces and viscous drag forces faced by magnetic microrobots, fabrication of MEMS devices with integrated hard magnetic materials and position sensing of the microrobot for intraocular applications. A new active defocused tracking method is proposed for visually servoing the microrobot in 3D using only a single microscope view.

1 Introduction

The state-of-the-art in MEMS technology is progressing from individual, chip-level microsensor and microactuator devices to complete integrated microrobot systems. These types of systems will impact future minimally invasive surgical techniques by providing sub-mm untethered biomedical microrobots capable of performing a number of procedures. The benefit will be even less injury to the patient resulting in correspondingly faster recovery times. Proven MEMS technologies such as micro-needles, micro-pumps and force and chemical sensors will be carried on-board for

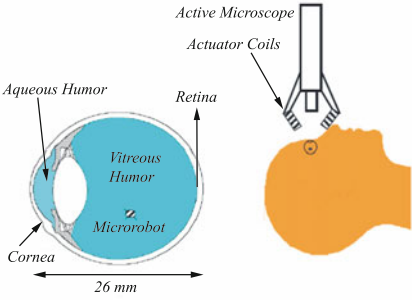

Fig. 1. The vitreous humor is a transparent, viscoelastic substance that occupies a large portion of the eyeball. Controlled magnetic fields are created by a set of coils to steer the microrobot inside the vitreous while an active microscope provides real-time 3D position feedback.

M.H. Ang and O. Khatib (Eds.): Experimental Robotics IX, STAR 21, pp. 321–330, 2006.

a variety of surgical and diagnostic tasks. Possible areas of application for these microrobots include cardiovascular, intraocular and inner-ear diagnosis and surgery.

Although electronic and mechanical systems have been miniaturized by VLSI and MEMS technologies, no counterpart to these exists for electro-chemical energy storage. Therefore, the only viable option for the actuation and steering of such a microrobot is external energy transfer. The use of magnetic fields generated ex-vivo for energy transfer and actuation can provide a solution to this problem.

This paper investigates some of the fundamental design issues related to magnetically actuated microrobotic systems. The nature of magnetic and viscous drag forces are analyzed. The advantages of using hard magnetic materials and fabrication methods for their integration into MEMS are discussed. Another major challenge is to create a suitable sensing technology to track the position of the microrobot inside the body. Different sensing methods will be better suited for application in different parts of the body, for example, magnetic or ultrasound sensing for cardiovascular microrobots and vision for intraocular applications. In this paper we also present a vision based sensing system to track the 3D position of a microrobot inside the eye. This system uses a single optical microscope to obtain a purposely defocused view of the microrobot to unambiguously resolve depth information.

2 Wireless Actuation Through Ex-Vivo Magnetic Fields

2.1 Nature of Magnetic Forces

The primary vectors that define the magnetostatic field in magnetized matter are (external) magnetic field strength, $\boldsymbol{H}$ (A/m), magnetization of the matter $\boldsymbol{M}$ (A/m) and magnetic flux density $\boldsymbol{B}$ (Tesla). The relationship between these vectors is

$$\boldsymbol{B} = \mu_0(\boldsymbol{H} + \boldsymbol{M}) \tag{1}$$

where μ_0 is the magnetic permeability of free space defined as $4\pi \times 10^{-7}$ Tm/A. For the idealized case of linear, isotropic and homogeneous media the following relationships simplify (1) as

$$\boldsymbol{M} = \chi \boldsymbol{H} \tag{2}$$

$$\boldsymbol{B} = \mu_0(1 + \chi)\boldsymbol{H} = \mu_0\mu_r\boldsymbol{H} \tag{3}$$

where χ and μ_r are the susceptibility and relative permeability of the media, respectively. In general, these values are not constant but change with magnetization, approaching zero as the magnetization reaches a material dependent limit called the *saturation magnetization* M_s. Within the saturation limits, the permeability can be thought as an amplification factor that creates a net magnetic field inside the matter through an external field.

Ferromagnetic materials exhibit the largest relative permeability (on the order of $10^3 - 10^5$). The dependence of magnetization on external fields (i.e. the M-H curve) for a ferromagnetic material is shown in Figure 2. The non-linear response

of the material also changes with its previous state of magnetization (indicating hysteresis). A ferromagnetic material magnetized to saturation will keep part of its magnetization (M_r, *remanent magnetization*) after the magnetizing field is taken away. It is necessary to apply a field H_{ci} (*intrinsic coercivity*) in the opposite direction of magnetization to cancel this magnetization. Soft magnetic materials (e.g. iron) are characterized by their high permeability and low coercivity ($H_{ci} < 10^3$ A/m) such that they can be easily magnetized and demagnetized by external fields. Hard magnetic materials (e.g. permanent magnets), on the other hand, have lower permeability but high coercivity ($H_{ci} > 10^4$ A/m), therefore, once magnetized, they retain their magnetization against external fields.

The magnetic force and torque that are exerted on an object with uniform magnetization $\boldsymbol{M}$ in a magnetic field with flux density $\boldsymbol{B}$ are defined as

$$\boldsymbol{F_m} = V_m(\boldsymbol{M} \cdot \nabla)\boldsymbol{B} \tag{4}$$

$$\boldsymbol{\tau_m} = V_m \boldsymbol{M} \times \boldsymbol{B} \tag{5}$$

where V_m is the volume of the magnetized object. Notice that the magnetic torque is dependent on $\boldsymbol{B}$ whereas the magnetic force is dependent on the gradient of $\boldsymbol{B}$. Equations (4) and (5) indicate that magnetic forces are volumetric. Therefore, the required fields and field gradients to exert a certain torque and force on a magnetized object increase rapidly as the object gets smaller.

2.2 Analysis of Required Magnetic Fields

Other than the magnetic forces analyzed above, gravitation/bouyancy and fluid drag forces are also acting on the microrobot. The drag force can be expressed as

$$F_d = 1/2 C_d \rho_f A \nu^2 \tag{6}$$

where ρ is the density of the body fluid, A is the cross sectional area of the robot, ν is the relative velocity of the robot with respect to the fluid media and C_d is the drag coefficient representing the overall effect of the robot's geometry on the drag force. A simplified analysis can be made assuming a spherical shape for the microrobot in which case (6) becomes

$$F_d = 3\pi\eta_f D\nu \tag{7}$$

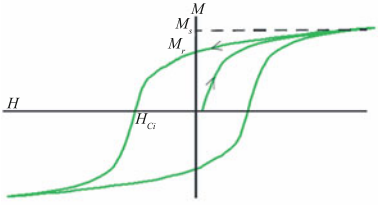

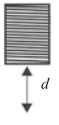

$\boldsymbol{H}_{solenoid} \sim \frac{1}{d^2}$ $\quad \boldsymbol{M} = \chi \boldsymbol{H} \sim \frac{1}{d^2}$

$\boldsymbol{B} = \mu_0 \mu_r \boldsymbol{H} \sim \frac{1}{d^2}$ $\quad \nabla \boldsymbol{B} \sim \frac{1}{d^3}$

$\boldsymbol{\tau_m} \sim \frac{1}{d^4}$ $\quad \boldsymbol{F_m} \sim \frac{1}{d^5}$

Fig. 2. Typical M-H curve of a ferromagnetic material. The force and torque on a magnetic object created by a solenoid coil.

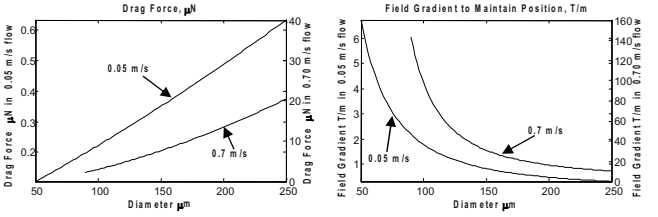

Fig. 3. Drag forces on a spherical magnet in the human blood and the required field gradient to resist the fluid drag for various sphere diameters. Plots for two different flow velocities (0.05 and 0.7 m/s) are shown. Note the different scales of the two plots.

where D is the diameter of the sphere and η_f is the fluid viscosity. In addition to the drag force, a net buoyancy force will be acting on the robot

$$F_b = V_r(\rho_r - \rho_f)g \tag{8}$$

where V_r and ρ_r are the density and volume of the robot respectively and g is the gravitational acceleration. The most important outcome of (4), (5), (6) and (8) is that, whereas magnetic and buoyancy forces are volumetric, the fluid drag forces are dependent on the area. For this reason, as the size of the robot gets smaller the required field gradient to move at a particular speed rapidly increases.

For cardiovascular applications, the fluid media that the microrobot moves in will be blood. The flow velocity of blood in the human body ranges between 0.05 m/s in the capillaries to 0.7 m/s at the exit of the aorta and viscosity of about 2.8 cP (centipoise) [11]. Figure 3 show the drag forces on a spherical permanent magnet with a diameter between 50 to 250 μm and magnetization $\boldsymbol{M} = 2.4 \times 10^4$ A/m (a reasonable value for deposited hard magnetic films on MEMS devices [9]) are plotted. The two extremes of blood flow velocity are considered in the two plots. In addition, the necessary field gradients to maintain position against the flow (i.e. balance the drag forces) are also shown.

The human eye, mostly filled by a transparent gel-like fluid called the vitreous humor, is another challenging workspace for a biomedical microrobot. The vitreous humor fills the posterior cavity of the eye between the lens and the retina (Figure 1) [12]. Although it is composed almost entirely of water (99%) it also contains a collagen fiber network, hyaluronic acid and soluble proteins, and, therefore, has the properties of a viscoelastic liquid with high viscosity. Viscoelastic materials can modeled by spring and dashpot elements representing the elastic and viscous characteristics of the material with shear modulus G and dynamic viscosity η. Two common models of viscoelastic behavior are the Maxwell and Kelvin elements that consist of a spring and a dashpot in series and in parallel, respectively (Figure 4).

A research study utilizing a specially built magnetic-bead rheometer device that performed non-destructive testing inside the eye has been reported by Lee et al [13][14]. Lee uses the Burgers model that consists of a Maxwell and Kelvin element in series to describe the properties of the vitreous (Figure 4a). Of the four parameters

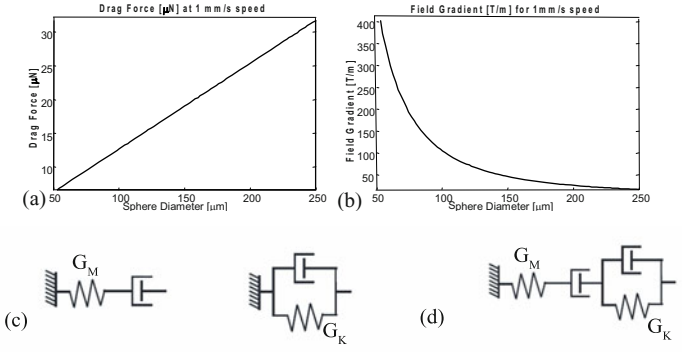

Fig. 4. a) and b) Drag forces on a spherical magnet moving at 1 mm/s in the human vitreous and the required field gradient for various sphere diameters. Magnetization is $\boldsymbol{M} = 2.4 \times 10^4$ A/m and viscosity is 1398 cP. c) Maxwell and Kelvin elements for decribing the rheological properties of materials. d) Burgers model used by Lee et al. [13] to model the vitreous humor.

in this model, the viscosity of the Maxwell dashpot (η_M) represents the irreversible flow of the material under constant stress that is the main source of the viscous drag forces on the robot as it is steered inside the eye. The mean values of viscosity were 1398 cP at the anterior, 2179 cP at the central and 4862 cP at the posterior regions. The values for the Kelvin viscosity were 4 to 10 times lower, further indicating the dominance of Maxwell viscosity for the drag force. Figure 4 shows the drag forces on a spherical permanent magnet with a diameter between 50 to 250 μm and magnetization 2.4×10^4 A/m moving inside the vitreous at a speed of $1mm/sec$. The mean viscosity at the anterior region is used. In addition, the necessary field gradient to balance the drag forces are also shown.

2.3 Actuation Through Magnetic Fields

Equations (4) and (5) suggest that controlled external magnetic fields can be used to induce torques and forces on a magnetized object and control its orientation and position. At the micro scale, active control and steering of magnetic beads in two and three dimensions have been demonstrated for DNA micromanipulation [6] and for performing intracellular rheology and force measurements [4] [5]. Whereas ferromagnetic materials exhibit higher susceptibility and saturation magnetization, the control of the beads' magnetization vector by external fields is difficult due to the hysteresis effect. Also, undesired interactions between magnetized beads can occur even after the external field has vanished. Superparamagnetic beads, which do not show hysteresis, are often used instead. The susceptibility of these beads, however, is much lower than ferromagnetic materials (e.g. 10^{-2} for commonly used M280 beads from Dynal Inc. [4]). Solenoid electromagnets with soft magnetic poles are typically used to generate high field gradients as much as 100 T/m across a 20 mm air gap [6].

An important issue related to the control of a magnetic microrobot is the nonlinear nature of the field and gradients that are created by electromagnet coils. The field from an aircore solenoid coil along its axis is roughly proportional to the inverse square of the distance d to the solenoid. In this case the torque and force on the soft magnetic material are proportional to the fourth and fifth inverse power of the distance respectively, as shown in Figure 2.

One way of reducing the effect of such nonlinearities is to create uniform magnetic fields and field gradients using various coil configurations [10]. For example, the Helmholtz coil configuration consists of two identical coils that are placed on the same axis and separated by a distance equal to the radius of the coils. This arrangement generates a uniform field close to the center of the coil pair when current passes in the same direction in both coils. Similarly, the Maxwell coil configuration can generate a uniform gradient near the center when the coils are separated by $\sqrt{3}$ times the radius and the current passes in the opposite direction. Figure 5 shows the plot of the fields of Helmholtz and Maxwell coils. Both of these coils are commonly used in MRI systems. Although, the uniform fields of commercial MRI machines are quite high (0.5-2.0 T), the gradient fields they can generate continuously are in the 0.01 to 0.05 T/m range.

3 Fabrication of MEMS with Integrated Hard Magnetic Materials

Material choices can also have an effect on the non-linear effects mentioned above. The magnetization vector in a hard magnetic material is not as dependent on external magnetic fields as it is in soft materials. In a soft magnetic material the magnetization vector follows the direction of the external field (within the energy limits set by the shape anisotropy effects). Therefore, neither the directionality nor the magnetization of the device is fixed. However, soft magnetic materials with saturation magnetizations up to 19×10^5 A/m can generate larger forces when operated at saturation.

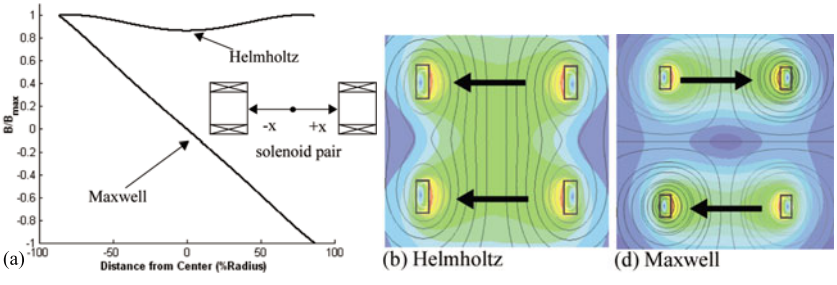

Fig. 5. a) Normalized magnetic field magnitudes along the central axes of Helmholtz and Maxwell coils. b) and c) Magnetic field and flux lines for Helmholtz and Maxwell coils, respectively. Arrows indicate the direction of current in the coils.

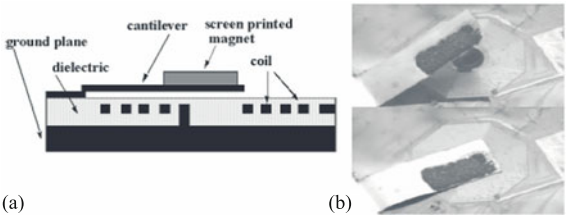

Fig. 6. Magnetically actuated cantilever device using screen printed NdFeB magnetic paste. a) Crossection of the device b) The cantilever is actuated by passing current through the 40 turn coil.

The ability to assign a direction to the robot is critical for accomplishing tasks with onboard tools and actuators.

A variety of techniques have been proposed for integrating hard magnetic materials into MEMS devices, including sputtering, thermal evaporation, assembly, electroplating, screen printing, spin coating and molding. Each method offers its own advantages and disadvantages. Our recent work [9] on integrating NdFeB magnetic powder into MEMS devices by wafer-level processing has resulted in magnets that have larger thickness (thus volume) and are stronger than thin film magnets. The screen printed magnets were fabricated using commercially available magnetic powder (Magnequench, MQP-S-9-8). The M_r value for the screen printed magnets was measured to be 2.4×10^5 A/m. A magnetically actuated thin film cantilever was built with screen printed magnets to demonstrate their integration with microfabrication processes. Figure 6 illustrates the device.

4 Microrobot Position Sensing Through Active Defocused Visual Tracking

Optical microscopes are commonly used to provide feedback for magnetic guidance of particles inside cells and other biological media [6][4]. These systems, however, operate only in 2D. In [5], a 3D magnetic bead steering system that used a laser light scattering technique to provide high bandwidth (10 kHz) position feedback was developed. Unfortunately, this technique is not suitable for tracking the intraocular microrobot since it requires a through path (i.e. not reflected) between the laser source and the photonic sensor element. The location of the eye inside the head does not allow such access. Although multi-camera methods with microscopes can provide precise 3D position information in real-time [15], these methods are also not suitable in this case since only a small window (i.e. the iris) is available for seeing inside the eye such a configuration is not possible.

Depth from focus/defocus methods are commonly used in microscopic vision to resolve the position of objects along the view-axis [16][17]. Depth from focus methods use a visual metric of image sharpness to detect whether regions of interest are in focus as the focus point of the microscope lens is moved along the optical axis

in controlled increments. This way the relative distance of two points at different depths can be found by determining where along this focal scan the points are in best focus as illustrated in Figure 7. Due to the necessary scanning motion this method is not applicable in real-time. An alternative is the depth from defocus method which uses the focus measure response directly to make measurements of distance to the plane of best focus. However, due to the symmetry of the focus measure curve about the plane of best focus, there are two depths corresponding to the same focus measure except at optimum focus. This problem can be solved using two cameras which share the same view through image splitting optics but at different planes of focus [18].

For 3D position tracking of the magnetic microrobot a third strategy has been developed that combines the high depth sensitivity of the depth from defocus method with an increased range of measurement and uses only a single microscope. The *active defocused tracking* method uses a microscope system that is actively servoed along the view axis to keep the target object (i.e. the microrobot) in a mid-level of defocus *at one side of the focus measure curve* (e.g. point B in Figure 7). This way a calibrated focus measure curve can be used to resolve the distance of the target to the plane of best focus, E_C, in real-time (i.e. at camera frame rate). This position error is added to the position of the microscope along the view axis, P_C, which can be measured by a linear encoder on the microscope stage. The resulting position error is used in the feedback loop that controls the external magnetic field and steers the microrobot inside the eye. A second feedback loop uses the defocus error, E_B, to servo the microscope stage so that the target object is kept at a mid-level of focus (Figure 8d).

The defocus tracking method was successfully implemented. A Sutter MP-285 micropositioning stage was used to actuate a microscope lens and a digital video camera whereas an identical stage was used to carry a target object. The target is a small piece of retroreflective tape that contains microspheres that reflect incoming light parallel to the direction of incidence. Figure 8 shows screen shots of the visual

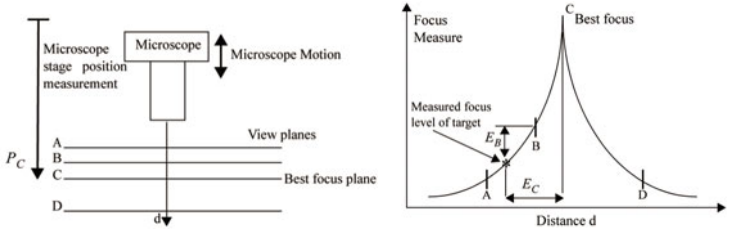

Fig. 7. A suitable measure of image focus reaches its maximum value when the reqion of interest is in best focus and decreases monotonically as the distance changes on either side of the best focus plane. The distance of a target to the best focus plane can be resolved from this curve if the target is always kept in defocus at one side of the curve by actively servoing the microscope stage.

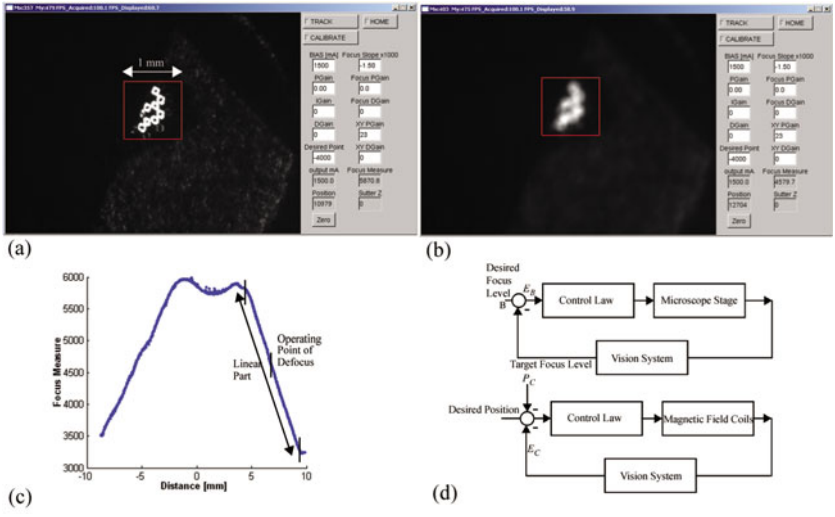

Fig. 8. a) and b) Screen shots of the active defocused tracking program showing the retroreflective target object in best focus and in mid level focus. c) The variance of grayscale values as a focus measure. During defocused tracking the target is actively kept at the center of the linear portion of this curve. d) Two separate control loops are used for the tracking and guidance of the microrobot.

tracking program with the target object at the best focus and in the mid-focus plane. A 2D tracking algorithm that uses simple thresholding and centroid calculation was used to detect the location of the target in the image taking advantage of the high contrast presented by the retroreflective target.

Defocusing is essentially a low-pass filtering operation, therefore, the amount of high frequency components in the area of interest is an indicator of image focus. In this work, the variance of the grayscale values inside the target area was used as the focus measure which created a linear response away from the best focus plane, as shown in Figure 8c. Note that this particular measure and target did not create a sharp peak at the best focus plane, however, the active defocused tracking method is not effected by this.

5 Conclusions

Magnetic actuation is a suitable mode of energy transfer for untethered biomedical microrobots. The improportional scaling of magnetic and viscous drag forces dictates the need for higher gradient magnetic fields over larger areas than are currently available with commercial MRI systems. For intraocular microrobots, limited physical access to the eye creates additional challenges for actuation and sensing. A real-time 3D visual tracking method using an active microscope that is suitable for visually servoing the position of the microrobot inside the eye was presented.

References

1. U. Hafeli, W. Schutt, J. Teller, M. Zborowski (ed), *Scientific and Clinical Applications of Magnetic Carriers*, NewYork: Plenum, 1997.
2. D.L. Holligan, G.T. Gilles, J.P. Dailey, "Magnetic Guidance of Ferrofluidic Nanoparticles in an In Vitro Model of Intraocular Retinal Repair", *IOP Nanotechnology*, vol. 14, pp. 661–666, 2003.
3. M. Zborowski,"Physics of Magnetic Cell Sorting", in Hafeli, Schutt, Teller, Zborowski et al., *Scientific and Clinical Applications of Magnetic Carriers*, NewYork: Plenum, pp. 205–232, 1997.
4. F. Amblard, B.Yurke, A. Pargellis, S. Leibler, "A Magnetic Manipulator for Studying Local Rheology and Micromechanical Properties of Biological Systems", *Review of Scientic Instruments*, vol. 67, no. 3, pp. 818–827, 2000.
5. L. Vicci, *A 3D Magnetic Force Manipulator DC Prototype*, UNC Chapel Hill Dept. Of Computer Science Technical Report, no. TR01-031, 2001.
6. C. Haber, D. Wirtz, "Magnetic Tweezers for DNA Micromanipulation", *Review of Scientic Instruments*, vol. 7, no. 12, pp. 4561–4570, December 2000.
7. K. Ishiyama, K.I. Arai, M. Sendoh, A. Yamazaki, "Spiral-type Micromachine for Medical Applications", *Proc. 2000 International Sym›posium on Micromechatronics and Human Science*, pp. 65–69, 2000.
8. J. Mathieu, S. Martell, L.Yahia, G. Soulez, G. Beaudoin, "Preliminary Studies for Using Magnetic Resonance Imaging Systems as a Mean of Propulsion for Microrobots in Blood Vessels and Evaluation of Ferromagnetic Artefacts", *IEEE CCECE Conf. on Elec. and Comp. Eng.*, pp. 835–838, 2003.
9. K. Vollmers, R. Anderson, B.J. Nelson, J. Pepin, "High Strength Rare Earth-Iron-Boron Printed Magnets Used In A Long Throw-High Force Electromagnetic Actuator With Microfabricated Coil", *IEEE Int. Conf. on MEMS (MEMS2003)*, pp. 60–63, 2003.
10. J. Jin, *Electromagnetic Analysis and Design in Magnetic Resonance Imaging*, Florida: CRC Press, 1999.
11. A. Despopoulos, S. Silbernagl, *Color Atlas of Physiology*, NewYork: Thieme Medical Publishers, pp. 156, 1991.
12. T.V. Chirilla, Y. Young, "The Vitreous Humor", *Handbook of Biomaterial Properties*", J. Black and G. Hastings et al., Chapman& Hall, London, 1998.
13. B. Lee, M. Litt, G. Buchsbaum, "Rheology of the Vitreous Body. Part I: Viscoelasticity of Human Vitreous", *Biorheology*, vol. 29, pp. 521–533, 1992.
14. B. Lee, *Comparative Rheological Studies of the Vitreous Body of the Eye*, Ph.D. Thesis, University of Pennsylvania, 1992.
15. K.B. Yesin, B.J. Nelson, "Robust CAD Model Based Visual Tracking for 3D Microassembly Using Image Space Potentials", *IEEE International Conference on Robotics and Automation*, 2004.
16. S. Allegro, C. Chanel, J. Jacot, "Autofocus for Automated Microassembly Under a Microscope", *IEEE Int. Conf. on Image Processing*, vol. 1, pp. 677–680, 1996.
17. B. Vikramaditya, B.J. Nelson, "Visually Guided Microassembly Using Optical Microscopes and Active Vision Techniques", *IEEE Int. Conf. on Robotics and Automation*, pp. 3172–3177, 1997.
18. S.K. Nayar, M. Watanabe, M. Noguchi, "Real-Time Focus Range Sensor", *IEEE Transactions on Pattern Analysis and Machine Intelligence*, vol. 18, no. 12, pp. 1186–1198, 1996.